ELSEVIER

Debonding of FRP plated concrete:
A tri-layer fracture treatment

Ching Au, Oral Büyüköztürk *

Massachusetts Institute of Technology, Cambridge, MA 02139, United States

Abstract

A tri-layer interface fracture energy model is developed to facilitate the quantification of various debonding scenarios in fiber reinforced polymer (FRP)/epoxy/concrete plated systems. The work is motivated by the relatively thick adhesive bond line generally encountered in such retrofitted systems. With the explicit material and geometric descriptions and the fairly general boundary conditions, the model provides a basis for parametric study and modeling of debonding in different specimen configurations. Comparison of the derived model specialized for peel and shear debonding with results from finite element modeling demonstrates the robustness of the derived model as an effective means to investigate FRP debonding as a basis for design.
© 2005 Elsevier Ltd. All rights reserved.

Keywords: Concrete; Debonding; FRP; Interface; Tri-layer

1. Background

Fiber reinforced plastic (FRP) materials are now broadly consumed in civil infrastructure applications including concrete internal reinforcements, pre- and post-stressing tendons, external strengthening and repair, and all-composite structural systems. In particular, FRP strengthening and repair of reinforced concrete (RC) elements such as beams, slabs, and bridge decks have been predominant owing to the increasing number of substandard structures as a result of design code revision, physical aging, seismic events, environmental deterioration, and inadequate maintenance.

---

* Corresponding author. Tel.: +1 617 253 7186; fax: +1 617 253 6044.
 E-mail address: obuyuk@mit.edu (O. Büyüköztürk).

For flexural strengthening, lightweight FRP laminates in the form of plates and sheets are often bonded to the soffits of the RC elements using a thixotropic ambient-cured epoxy that is designed for in situ overhead applications. These epoxy materials are thicker than most elevated-temperature cured epoxy commonly found in aerospace applications and usually have a bond line thickness of the same order as the FRP laminate itself, which ranges mostly from 0.5 mm to 2 mm. In some cases, the epoxy manufacturers pre-process the epoxy and hardener components into a solid base material to provide better troweling capability.

Large-scale retrofitted RC beam tests [36,4,6,16,15] indicate that failures of FRP plated systems may take place through various possible mechanisms, depending on the concrete grade, rebar provision, properties of FRP, and service environments. Identified failure modes include: (1) concrete crushing before steel yielding; (2) steel yielding followed by concrete crushing; (3) steel yielding followed by FRP rupture; (4) shear failure; (5) concrete cover delamination; and (6) debonding in the vicinity of the FRP/epoxy/concrete bond interface.

In particular, debonding of FRP plated concrete has been considered a challenging failure mode for analysis and design. Debonding is often observed at discontinuities such as laminate ends and existing crack mouths within the retrofit span [28,17] where high concentration of shear and peel stresses can be found [33]. With the advent of various anchorage techniques [32,12,13,25,24,33,16], however, debonding locations have been forced to take place within the retrofit span where debonding is initiated by crack widening and differential vertical movements of the crack mouths induced by external loading [33].

From short-term tests [7,34,2,23,31,26,30,9,37,11] and environmental durability tests [8,35,22,29,15,1,21] on FRP bonded concrete systems, which consist of three constituent materials (FRP, adhesive, and concrete) and two interfaces, that are subjected to peel, shear, and flexural loading, it is now known that debonding may occur as one of five possible modes as illustrated in Fig. 1. They are namely (1) FRP delamination, (2) FRP/adhesive separation, (3) adhesive decohesion, (4) adhesive/concrete separation, and (5) concrete substrate fracture, depending on the FRP and epoxy used, properties of the concrete substrate, as well as environmental effects the retrofitted system is subjected to.

The five failure modes can broadly be classified as two classes of failure: (a) material decohesion and (b) interface fracture. Failures (1), (3), and (5) are considered material decohesion while failures (2) and (4) are considered interface fracture. Among the five debonding modes, concrete delamination has been the most observed [33]. The cause of such is generally explained by the concrete property as representing the weakest and most brittle material in the interfacial bond region. Other failures such as FRP delamination and adhesive decohesion have also been observed but do not appear as frequently. Interface separation modes such as FRP/adhesive separation and adhesive/concrete separation are generally not observed in short-term tests [14], but have recently been discovered to associate with moisture-affected systems [22,1,21].
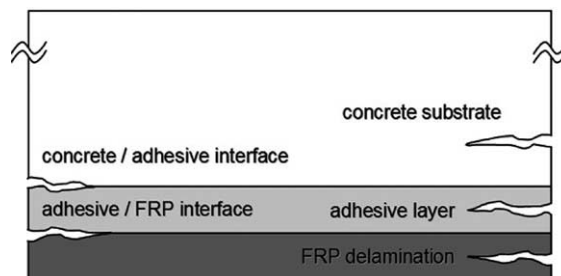

Fig. 1. Five possible debonding modes.

2. Need for tri-layer interface fracture quantification of debonding

While a large number of experimental and theoretical investigations have been carried out to study debonding in FRP retrofitted concrete systems, the debonding mechanics is generally not well understood due in part to the inherently less explicit strength-based approach frequently adopted. Debonding, which is an interface fracture problem by nature, may involve material decohesion and/or interface separation. Unlike material decohesion (e.g. concrete delamination) of which debonding failure occurs as a result of material limits being utilized, interface separation is a debonding mode that is governed by the adhesion property of the adjoining constituent materials such that material limits are not necessarily attained. While the strength approach is capable of quantifying and analyzing material decohesion type of debonding, it intrinsically lacks the ability to describe adhesion related phenomenon. As such, debonding resistance of a FRP retrofitted concrete element may be better quantified by an interface fracture toughness parameter that can be considered a bond property.

As discussed earlier, five distinct failure modes are possible. These different failure modes can be clearly observed by visual analysis due partly to the fact that the adhesive bond line thickness in such retrofitted systems is relatively large. To characterize these different debonding modes, an interface fracture model that contains parametrically the material and geometric information of all three constituent materials of the bonded system is needed. While bi-layer fracture models [20,5,3] are capable of describing other layered systems with negligible bond line thickness such as protective coating, electronic packages, capacitors, and general thin-film/substrate systems, a new tri-layer fracture model needs to be developed to sufficiently describe the FRP debonding problems in FRP-plated systems, which involve FRP, epoxy, and concrete layers. For FRP sheet systems, however, the bond line might not be as clearly distinguished.

It is the objective of this paper to derive five idealized general tri-layer debonding models that can be used to quantify the debonding problem of FRP plated concrete. The models are linear elastic and are derived based on energy arguments combined with the classical beam theory. These solutions provide a rigorous quantification of the total interface fracture energy release rate of the bonded system and represent a further development of the bi-layer fracture energy models that are presented in Hutchinson and Suo [20]. The models are developed with fairly general boundary conditions so that they can be specialized for describing different physical models such as the peel and lap shear models frequently used in studying debonding of FRP retrofitted concrete systems at the meso-scale.

3. Energy considerations

Debonding in a FRP bonded concrete system is a complex phenomenon. As the parent crack propagates at or near the bond interface, various energy dissipation mechanisms may take place. Some possible mechanisms include the release of elastic strain energy buildup in the bond during fracture (i.e. when new fracture surfaces are generated), non-linear elastic, viscoelastic, or plastic behavior of the adhesive bond line depending on the material and service conditions, frictional effect at interfaces due to mechanical interlocking, and microcracking in the concrete substrate. The total amount of energy dissipated during debonding, D, can thus be expressed as the sum of the work of separation, γ_s, that is responsible for generating new fracture surfaces and all the other energy dissipative mechanisms, γ_d, over the area of debonding dA

$$D = \int \gamma_s \, dA + \int \gamma_d \, dA \tag{1}$$

For fracture to occur, the energy release, $\int G \, dA$, should be greater than or equal to the total amount of energy dissipated.
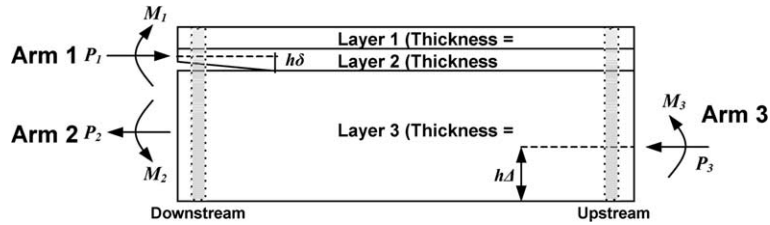
Fig. 2. Model idealization and definition for debonding between layers 2 and 3.

$$\int G \, \mathrm{d}A \geqslant D \tag{2}$$

In the case of fracture under prescribed load, the total potential of the bonded system, Π, is related to the elastic strain energy U and potential energy due to external loads V as follows:

$$\Pi = U - V \tag{3}$$

Consider a linear elastic assumption for first order analysis as in most fracture problems, where $V = 2U$ exactly. Therefore, at fracture

$$\mathrm{d}\Pi = -\mathrm{d}U \tag{4}$$

Hence, the fracture energy release rate, G, is expressed as follows:

$$G = -\frac{\mathrm{d}\Pi}{\mathrm{d}A} = \frac{\mathrm{d}U}{\mathrm{d}A} = \mathrm{d}(U_\mathrm{d}) \tag{5}$$

where U_d is the strain energy per unit length per unit width of the bonded system. In other words, for interface fracture to occur at the steady state [19], the amount of energy dissipated in creating a new interface crack, $\mathrm{d}D$, should equal the change in elastic strain energy due to cracking (i.e. strain energy release). The fracture energy release rate G is thus the difference between U_d of a cracked body (far behind the crack tip or downstream) and that of an intact body (far ahead the crack tip or upstream), as illustrated in Fig. 2 for a debonding problem where an interface crack exists between Layer 2 and Layer 3.

$$G = (U_\mathrm{d})_\mathrm{downstream} - (U_\mathrm{d})_\mathrm{upstream} \tag{6}$$

As such, G can be computed exactly by evaluating the strain energy per unit width per unit length of the bonded system, which contains a crack in an arbitrary location near the bond interface, using the classical beam theory. The solutions for this tri-layer problem can be algebraically cumbersome and thus non-dimensional area and moment of inertia are carefully chosen for systematic tabulation.

4. Interface fracture models and solutions

The tri-layer interface fracture energy release rate models (hereafter called G models) are derived in accordance to the energy principles described in the previous section. For a tri-material layered system, there are altogether five possible fracture scenarios, two being interface separation and three material decohesion, as previously presented. Each of the debonding modes is idealized and defined in Fig. 3 for derivation purposes. Table 1 summarizes the interface fracture cases and the corresponding debonding modes in case of a FRP bonded concrete system with respect to the case numbers of the idealized models.

Each of the five derived G models can be used to compute the interface fracture energy release rate that corresponds to the observed debonding mode from experiments. Thickness for layer 1 (top) through 3 (bottom) is designated h, t, and H, respectively. Definitions of the normalized neutral axis locations α, α_3, δ, Δ, Δ_2, Δ_3, Δ_{33} of the composite arms can be found in Appendix A.
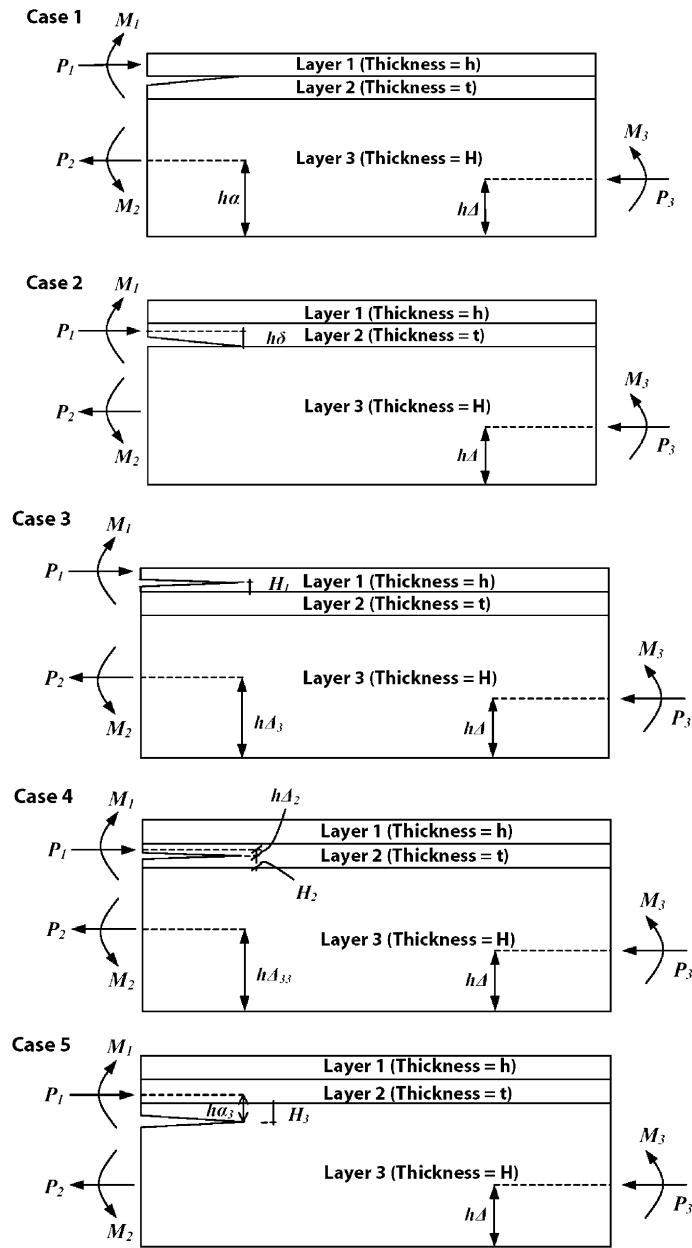
Fig. 3. Idealization and definition of all debonding scenarios.

4.1. Assumptions

Derivation of each idealized debonding model assumes that each of the three layers is homogeneous, iso-tropic, and linearly elastic. The uncracked interfaces are perfectly bonded with continuous displacements and tractions. The tri-material models are all loaded uniformly along the edges with constant forces (in

Table 1
Summary of G model cases

	Interface fracture mode	Corresponding debonding mode in FRP bonded concrete systems
Case 1	Interface separation between layers 1 and 2	FRP/adhesive interface separation
Case 2	Interface separation between layers 2 and 3	Adhesive/concrete interface separation
Case 3	Material decohesion of layer 1	FRP delamination
Case 4	Material decohesion of layer 2	Adhesive decohesion
Case 5	Material decohesion of layer 3	Concrete delamination

the form of stretching) and moments per unit width at the neutral axis of the respective composite arms. Plain strain condition is assumed, as the bond width is usually 1–2 orders of magnitude higher than the bond thickness.

4.2. Derivation

All five G models are developed using identical derivation procedures. In what follows, the derivation and solution of the Case 2 G model are first presented, followed by the generalized solution form that applies to all five cases and the tabulated results of the general terms for each case.

As discussed in the last section, the interface fracture energy release rate G can be obtained by computing the difference between the U_d of a cracked body (far behind the crack tip or downstream) and that of an intact body (far ahead the crack tip or upstream), as expressed by Eq. (6). Thus for Case 2, by referring to Fig. 2

$$G_{\text{Case 2}} = (U_d)_{\text{Arm 1}} + (U_d)_{\text{Arm 2}} - (U_d)_{\text{Arm 3}} \tag{7}$$

Each arm can be treated as a composite beam and the classical beam theory can be used to derive the expression for U_d for each particular arm. U_d is defined as the total elastic strain energy, U, per unit width per unit length of the bond. Hence, when constant load and moment are involved, U_d of a composite arm a can be expressed as follows:

$$U_d = \frac{P_a^2}{2(\overline{E}A)_{\text{Arm }a}} + \frac{M_a^2}{2(\overline{E}I)_{\text{Arm }a}} \tag{8}$$

where P_a is the constant load (stretch) per unit width acting on the neutral axis of the composite beam, M_a the constant moment per unit width applied about the same neutral axis, $(\overline{E}A)_{\text{Arm }a}$ the plain strain axial rigidity of the composite arm, and $(\overline{E}I)_{\text{Arm }a}$ the plain strain flexural rigidity. Now, the composite rigidities are developed for each arm.

4.2.1. Arm 1
For Arm 1, which is behind the crack tip, the neutral axis of the bi-layer composite beam is defined at a location $h\delta$ above the crack interface, where δ can be derived as follows:

$$\delta = \frac{\Sigma_{12} + 2\Sigma_{12}\frac{\gamma}{\eta} + \left(\frac{\gamma}{\eta}\right)^2}{2\left(\Sigma_{12} + \frac{\gamma}{\eta}\right)} \tag{9}$$

where

$$\Sigma_{ij} = \frac{\overline{E}_i}{\overline{E}_j} \tag{9a}$$

$$\overline{E}_n = \frac{E_n}{1 - v_n^2} \text{ for plain strain} \tag{9b}$$

$$\eta = \frac{h}{H} \tag{9c}$$

$$\gamma = \frac{t}{H} \tag{9d}$$

Here, E_n is the elastic modulus of material layer n, v_n the corresponding Poisson's ratio, i and j the material layer numbers which range from 1 to 3. The dimensionless cross-section area $A_{1,2}$ and moment of inertia $I_{1,2}$ for Case 2 are normalized with respect to the thickness of layer 1, h, and are expressed, respectively

$$A_{1,2} = \Sigma_{13} + \Sigma_{23}\frac{\gamma}{\eta} \tag{10}$$

$$I_{1,2} = \Sigma_{13}\left[\left(\frac{\gamma}{\eta}\right)^2 + (1 - 2\delta)\left(\frac{\gamma}{\eta}\right) + \frac{3(1 - 2\delta)^2 + 1}{12}\right] + \Sigma_{23}\left[\delta\left(\frac{\gamma}{\eta}\right)\left(\delta - \frac{\gamma}{\eta}\right) + \frac{1}{3}\left(\frac{\gamma}{\eta}\right)^3\right] \tag{11}$$

4.2.2. Arm 2

Arm 2 only consists of Layer 3 and thus the neutral axis coincides with the centerline of the layer, which is $H/2$ from the crack interface. So, the cross-section area $A_{2,2}$ and moment of inertia $I_{2,2}$ for Case 2 are, respectively

$$A_{2,2} = \frac{1}{\eta} \tag{12}$$

$$I_{2,2} = \frac{1}{12\eta^3} \tag{13}$$

4.2.3. Arm 3

Finally for Arm 3, which is far ahead of the crack tip, the tri-layer composite beam has a neutral axis defined at $h\Delta$ above the bottom of the beam, where Δ can be derived as follows:

$$\Delta = \frac{1 + \Sigma_{23}\gamma(2 + \gamma) + \Sigma_{13}\eta(2 + 2\gamma + \eta)}{2\eta(1 + \Sigma_{23}\gamma + \Sigma_{13}\eta)} \tag{14}$$

The dimensionless cross-section area $A_{3,2}$ and moment of inertia $I_{3,2}$ for Case 2 are, respectively

$$A_{3,2} = \Sigma_{13} + \Sigma_{23}\frac{\gamma}{\eta} + \frac{1}{\eta} \tag{15}$$

$$I_{3,2} = \Sigma_{13}\left[\left(\frac{1 + \gamma}{\eta} - \Delta\right)^2 + \left(\frac{1 + \gamma}{\eta} - \Delta\right) + \frac{1}{3}\right]$$
$$+ \Sigma_{23}\left[\left(\frac{\gamma}{\eta}\right)^3\left(\frac{1}{\gamma^2} + \frac{1}{\gamma} + \frac{1}{3}\right) + \left(\frac{\gamma}{\eta}\right)\left(\Delta - \frac{2 + \gamma}{\eta}\right)\right] + \frac{\Delta}{\eta}\left(\Delta - \frac{1}{\eta}\right) + \frac{1}{3\eta^3} \tag{16}$$

Combining, the interface fracture energy release rate, G, which specifies the total magnitude of the near-tip singularity for a Case 2 debonding, is expressed as follows:

$$G_{\text{Case 2}} = \frac{1}{2\overline{E}_3}\left[\frac{P_1^2}{A_{1,2}h} + \frac{M_1^2}{I_{1,2}h^3} + \frac{P_2^2}{A_{2,2}h} + \frac{M_2^2}{I_{2,2}h^3} - \frac{P_3^2}{A_{3,2}h} - \frac{M_3^2}{I_{3,2}h^3}\right] \qquad (17)$$

A limiting case of this solution is when layer 2 vanishes (i.e. $t \to 0$, hence $\gamma \to 0$). In such case, the above solution converges exactly to the bi-layer solution derived by Hutchinson and Suo [20].

Also note that the fracture model is in overall equilibrium when the edge loads and moments are related as follows:

$$P_1 - P_2 - P_3 = 0 \qquad (18)$$

$$M_1 - M_2 + P_1(h\delta + H - h\varDelta) + P_2\left(h\varDelta - \frac{H}{2}\right) - M_3 = 0 \qquad (19)$$

Here, the signs or directions of the loads and moments do not affect the value of G. However, this is not so when stress intensity factors, which are also expressed as a function of these external loads, are considered [19].

4.3. Generalized solutions

The expression of G presented above takes the general form

$$G_{\text{Case }k} = \frac{1}{2\overline{E}_3}\left[\frac{P_1^2}{A_{1,k}h} + \frac{M_1^2}{I_{1,k}h^3} + \frac{P_2^2}{A_{2,k}h} + \frac{M_2^2}{I_{2,k}h^3} - \frac{P_3^2}{A_{3,k}h} - \frac{M_3^2}{I_{3,k}h^3}\right] \qquad (20)$$

where the dimensionless cross-section areas $A_{i,k}$ and moment of inertias $I_{i,k}$ of each composite Arm i (from 1 to 3) are differently expressed for each debonding fracture scenario k (from 1 to 5) due to the different neutral axis position definitions as a result of the specific crack locations. Tables 2–4 summarize the

Table 2
Solutions of $A_{1,k}$ and $I_{1,k}$

Case	$A_{1,k}$	$I_{1,k}$
$k = 1$	Σ_{13}	$\dfrac{\Sigma_{13}}{12}$
$k = 2$	$\Sigma_{13} + \Sigma_{23}\dfrac{\gamma}{\eta}$	$\Sigma_{13}\left[\left(\dfrac{\gamma}{\eta}\right)^2 + (1-2\delta)\left(\dfrac{\gamma}{\eta}\right) + \dfrac{3(1-2\delta)^2+1}{12}\right] + \Sigma_{23}\left[\delta\left(\dfrac{\gamma}{\eta}\right)\left(\delta - \dfrac{\gamma}{\eta}\right) + \dfrac{1}{3}\left(\dfrac{\gamma}{\eta}\right)^3\right]$
$k = 3$	$\Sigma_{13}(1 - \xi_1)$	$\Sigma_{13}\dfrac{(1-\xi_1)^3}{12}$
$k = 4$	$\Sigma_{13} + \Sigma_{23}\left(\dfrac{\gamma}{\eta} - \xi_2\right)$	$\Sigma_{13}\left[\left(\dfrac{\gamma}{\eta}\right)^2 + (1-2\varDelta_2-2\xi_2)\left(\dfrac{\gamma}{\eta}\right) + \dfrac{3(1-2\varDelta_2)^2+1}{12} + \xi_2^2 - \xi_2(1-2\varDelta_2)\right]$
		$+ \Sigma_{23}\left[\varDelta_2\left(\dfrac{\gamma}{\eta}\right)\left(\varDelta_2 - \dfrac{\gamma}{\eta}\right) + \dfrac{1}{3}\left(\dfrac{\gamma}{\eta}\right)^3 - \dfrac{1}{3}\xi_2^3 - \xi_2^2\left(\varDelta_2 - \dfrac{\gamma}{\eta}\right) - \xi_2\left(\varDelta_2 - \dfrac{\gamma}{\eta}\right)^2\right]$
$k = 5$	$\Sigma_{13} + \Sigma_{23}\dfrac{\gamma}{\eta} + \xi_3$	$\Sigma_{13}\left[\left(\dfrac{\gamma}{\eta}\right)^2 + (1-2\alpha_3+2\xi_3)\left(\dfrac{\gamma}{\eta}\right) + \xi_3(1-2\alpha_3+\xi_3) + \dfrac{3(1-2\alpha_3)^2+1}{12}\right]$
		$+ \Sigma_{23}\left[\dfrac{1}{3}\left(\dfrac{\gamma}{\eta}\right)^3 + (\xi_3-\alpha_3)\left(\dfrac{\gamma}{\eta}\right)^2 + (\xi_3-\alpha_3)^2\left(\dfrac{\gamma}{\eta}\right)\right] + \xi_3\alpha_3(\alpha_3-\xi_3) + \dfrac{1}{3}\xi_3^3$

Table 3
Solutions of $A_{2,k}$ and $I_{2,k}$

Case	$A_{2,k}$	$I_{2,k}$
$k=1$	$\Sigma_{23}\dfrac{\gamma}{\eta}+\xi$	$\Sigma_{23}\left[\dfrac{1}{3}\left(\dfrac{\gamma}{\eta}\right)^3+(\xi-\alpha)\left(\dfrac{\gamma}{\eta}\right)^2+(\xi-\alpha)^2\left(\dfrac{\gamma}{\eta}\right)\right]+\dfrac{1}{3}\xi^3-(\xi-\alpha)\left(\dfrac{\alpha}{\eta}\right)$
$k=2$	ξ	$\dfrac{1}{12}\xi^3$
$k=3$	$\Sigma_{13}\xi_1+\Sigma_{23}\dfrac{\gamma}{\eta}+\xi$	$\Sigma_{13}\left[\dfrac{\xi_1^3}{3}+\xi_1^2\left(\dfrac{\gamma}{\eta}+\xi-\varDelta_3\right)+\xi_1\left\{(\xi-\varDelta_3)^2+\dfrac{\gamma}{\eta}\left(\dfrac{\gamma}{\eta}-2\xi-2\varDelta_3\right)\right\}\right]$ $+\Sigma_{23}\left[\dfrac{1}{3}\left(\dfrac{\gamma}{\eta}\right)^3+(\xi-\varDelta_3)\left(\dfrac{\gamma}{\eta}\right)^2+(\xi-\varDelta_3)^2\left(\dfrac{\gamma}{\eta}\right)\right]+\dfrac{\xi^3}{3}-\varDelta_3\xi(\xi-\varDelta_3)$
$k=4$	$\Sigma_{23}\xi_2+\xi$	$\Sigma_{23}\left[\dfrac{1}{3}\xi_2^3+(\xi-\varDelta_{33})\xi_2^2+(\xi-\varDelta_{33})^2\xi_2\right]+\dfrac{\xi^3}{3}-(\xi-\varDelta_{33})\xi\varDelta_3$
$k=5$	$\xi-\xi_3$	$\dfrac{(\xi-\xi_3)^3}{12}$

Table 4
Solutions of $A_{3,k}$ and $I_{3,k}$

Case	$A_{3,k}$	$I_{3,k}$
$k=1$ $k=2$ $k=3$ $k=4$ $k=5$	$\Sigma_{13}+\Sigma_{23}\dfrac{\gamma}{\eta}+\xi$	$\Sigma_{13}\left[\left(\dfrac{1+\gamma}{\eta}-\varDelta\right)^2+\left(\dfrac{1+\gamma}{\eta}-\varDelta\right)+\dfrac{1}{3}\right]$ $+\Sigma_{23}\left[\left(\dfrac{\gamma}{\eta}\right)^3\left(\dfrac{1}{\gamma^2}+\dfrac{1}{\gamma}+\dfrac{1}{3}\right)+\left(\dfrac{\gamma}{\eta}\right)\left(\varDelta-\dfrac{2+\gamma}{\eta}\right)\right]+\dfrac{\xi^3}{3}+\varDelta\xi(\varDelta-\xi)$

corresponding $A_{i,k}$ and $I_{i,k}$ for the three composite arms. Definitions of thickness, modulus, crack location, and neutral axis parameters are given in Appendix A.

5. FRP debonding in peel and shear fracture specimens

The generality of loading conditions for the models makes them applicable to many different classes of problems that involve a tri-layer material structure. For the purpose of studying debonding in FRP-adhesive-concrete systems, peel and shear characterization is often used due to the nature of the debonding problem within the retrofit span as illustrated in Fig. 4. The peel and shear loading represent the two limiting bounds. Fracture toughness values of these two bounds can be obtained by inputting the respective fracture loads (i.e. at the critical state) into the tri-layer G model for computation. In other words, the G model essentially transforms the strength-based test data into fracture-based quantities for analysis. Loadings from the specialized peel and shear models are expressed as the equivalent stretch P_i and moment M_i in the general solutions with adjustments made to the actual loading lines and will be illustrated, respectively, below for each loading case.
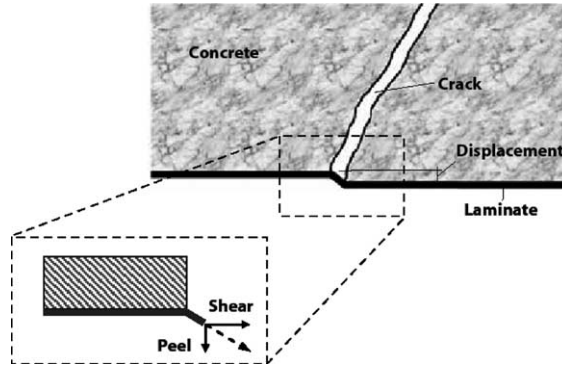
Fig. 4. Local debonding configuration at crack mouth location.

5.1. Solutions for debonding under shear

Fig. 5 illustrates a typical single lap shear FRP bonded concrete model that is commonly used in the characterization of effective bond length [2] and interfacial stresses [33] of FRP bonded concrete systems. A constant shear load, N_x, is applied horizontally to the FRP cantilever while a reaction plate pushes against the concrete block.

Comparing the loading line of *Arm 1* in Fig. 5 (i.e. N_x) with the loading line in all cases as shown in Fig. 3 (i.e. P_1), a constant bending moment, which comes from the eccentricity of the load, Ψ, exists, except Case 1. This is so due to the fact that the actual loading, N_x, is applied to the centerline of FRP laminate instead of the neutral axis of the composite *Arm 1*. For instance, the eccentricity that appears in Case 2 is

$$\Psi = t - h\delta + \frac{h}{2} \tag{21}$$

In all realistic applications, thickness of the concrete substrate is at least two orders of magnitude higher than that of both the FRP laminate and the epoxy layer (i.e. $H \gg h, t$) and hence, $\eta \to 0$ and $\gamma \to 0$. This leads the 3rd, 4th, 5th, and 6th terms in the general solution to vanish. Thus, only the first two terms of the generalized solution remain, i.e.

$$G_{\text{shear}} = \frac{1}{2\overline{E}_3} \left[\frac{P_1^2}{A_{1,2}h} + \frac{M_1^2}{I_{1,2}h^3} \right] \tag{22}$$
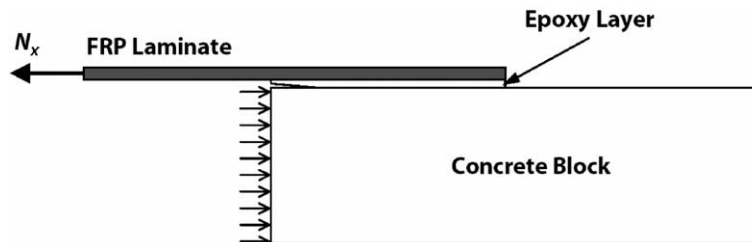

Fig. 5. Shear fracture model.

Now that $P_1 = \frac{N_x}{B}$ and $M_1 = \frac{N_x \Psi}{B}$ for a bond width B, the G_{shear} model can be expressed in the following form:

$$G_{\text{shear}} = \frac{N_x^2}{2B^2 \overline{E}_3} \left(\frac{1}{A_{1,2}h} + \frac{\Psi^2}{I_{1,2}h^3} \right) \tag{23}$$

Eccentricities, Ψ, for all five cases are summarized in Table 5.

5.2. Solutions for debonding under peel

Fig. 6 shows a typical peel fracture model where there is a constant peel load applied at the tip of the FRP cantilever, in which the bending moment increases linearly from the load application point to the crack tip, deviating from the assumed constant moment in the general solution presented above. As such, the U_d that accounts for a linearly increasing moment needs to be explicitly derived to replace the associated constant moment term in the general solution.

Using the same arguments for thickness differences of the material layers as in the shear case and exercising the fact that there is no horizontal stretching (i.e. $P_1 = 0$), only the 2nd moment term of the generalized solution remains. However, this constant moment term needs to be converted to a varying moment term which can account for the linearly varying moment that ranges from zero at the FRP tip at which the peel load, P, is applied, to $P(l + a)$ at the crack tip that is length a ahead of the edge of the concrete

Table 5
Eccentricities

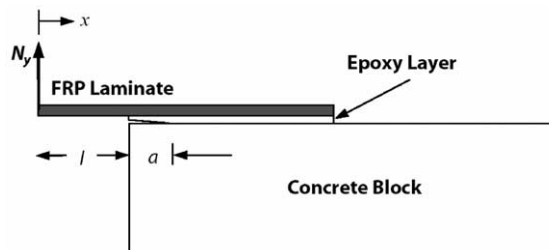| Case	Ψ
$k = 1$	0
$k = 2$	$h\left(\frac{1}{2} - \delta\right) + t$
$k = 3$	$\frac{H_1}{2}$
$k = 4$	$h\left(\frac{1}{2} - \Delta_2\right) + t - H_2$
$k = 5$	$h\left(\frac{1}{2} - \alpha_3\right) + t + H_3$

Fig. 6. Peel fracture model.

block. Here, P is defined as the peel load per unit width B, l the FRP cantilever length, and a the pre-crack length. To derive the expression properly, the overall U_d is evaluated over two sections. The first section computes only the U_d accumulated within the FRP cantilever (i.e. $x = 0$ to $x = l$) and the second section computes the U_d accumulated over the pre-crack length (i.e. $x = l$ to $x = l + a$). Let $I_{FRP} = h^3/12$ be the moment of inertia of the FRP cantilever, then

$$G_{\text{peel}} = \frac{\mathrm{d}}{\mathrm{d}(l+a)} \left(\int_0^l \frac{(Px)^2}{2\overline{E}_1 I_{FRP}} \, \mathrm{d}x + \int_l^{l+a} \frac{(Px)^2}{2\overline{E}_3 I_{1,2} h^3} \, \mathrm{d}x \right) \tag{24}$$

Integrating and differentiating accordingly, the G_{peel} solution associated with a constant peel load becomes

$$G_{\text{peel}} = \frac{N_y^2}{B^2 \overline{E}_3 h^3} \left(\frac{(l+a)^2 - l^2}{2 I_{1,2}} + \frac{6 l^2}{\Sigma_{13}} \right) \tag{25}$$

where N_y is defined as the total peel load over the bond width (i.e. $N_y = PB$).

6. Parametric study of the peel and shear fracture models

With the specialized models, parametric studies can be performed on critical parameters to develop an understanding of the debonding mechanics and on how debonding might be prevented through design. In particular, relative thickness and elastic mismatch of the bond line are of concern since the epoxy layer, which is produced on-site, is difficult to control for its uniformity and yet is responsible for stress transfer from the RC beam to the external FRP reinforcement. Thus, a parametric study is performed as part of this application using realistic material and geometric values.

As discussed at the onset of the G model derivations, the models describe only the total interface fracture energy without explicit consideration of the mixed-mode stress-intensities at the crack tip. As the nature of a multi-layer bonded system, mode-mix behavior would arise due solely to the elastic mismatch of the adjoining materials, even though the external loading and/or the model geometry are apparently symmetric [20]. It is thus important to evaluate the sensitivity of G to the elastic mismatch between the material layers. Elastic mismatch has often been characterized by the Dundurs' parameters [10]. Let Case 2 be the example problem; the Dundurs' parameters can then be defined between Layers 2 and 3 with the plain strain assumption as follows:

$$\alpha_{\text{Dundurs}} = \frac{\overline{E}_2 - \overline{E}_3}{\overline{E}_2 + \overline{E}_3} \tag{26}$$

$$\beta_{\text{Dundurs}} = \frac{1}{2} \frac{\mu_2(1 - 2v_3) - \mu_3(1 - 2v_2)}{\mu_2(1 - 2v_3) + \mu_3(1 - 2v_2)} \tag{27}$$

where α_{Dundurs} represents the mismatch in elastic modulus, β_{Dundurs} the mismatch in bulk modulus, μ_i the shear modulus of material layer i. Note here that α_{Dundurs} approaches $+1$ when the upper layer is comparatively very stiff while -1 when the layer is very compliant. Both α_{Dundurs} and β_{Dundurs} vanish when the elastic mismatch is absent. Also, α_{Dundurs} and β_{Dundurs} change signs when the material layers are switched. Fig. 7 shows the effect of elastic mismatch on G for both the shear and peel cases, using the α_{Dundurs} parameter. A practical range of epoxy layer thickness t (in mm) is considered. The magnitudes of l, a, h, and B used in the G computation are, respectively, 50 mm, 12.5 mm, 1.28 mm, and 25 mm.

It is shown in both loading cases that the larger the mismatch, the higher is the G value in either case, with stronger effect on the peel case. This means that when elastic mismatch between the epoxy and concrete layers is high, debonding at the interface is more likely to occur, given that the interfacial fracture energy remains unchanged. When α_{Dundurs} reaches about 0.8, the peel fracture energy release rate (a driving
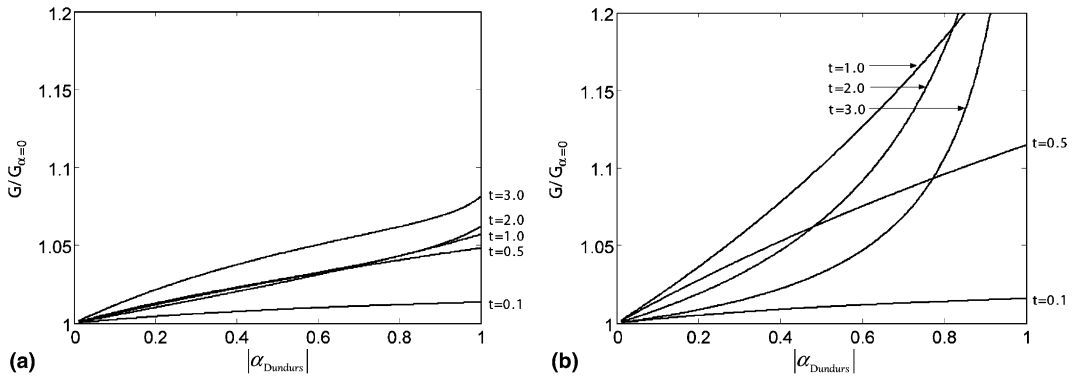
Fig. 7. Effect of elastic mismatch on (a) shear G and (b) peel G.

force for debonding), G_{peel}, would increase by more than 20% over the limiting value without any mismatch (i.e. $\alpha_{Dundurs} = 0$). It is also generally observed that the effect of elastic mismatch would diminish when the epoxy bond line thickness is reduced for a given FRP laminate thickness.

Owing to the nature of in situ bonding, uniformity of the bond line thickness can be difficult to control, especially for bonding over long span length. Thus, studying the effect of epoxy thickness could reveal how critical it is to control the bond line thickness and its uniformity. Fig. 8 shows the variation of $G/G_{t=0}$ as a function of t/h.

It is observed that for a given thickness of FRP laminate h, a thicker epoxy bond line would lower the fracture energy release rate at the interface crack tip, and hence is advantageous in mitigating the chances of debonding. Variation of the bond line thickness within the practical range would not induce variation in the fracture energy release for over 15%. At any given t/h ratio, a thinner FRP laminate would lead to a larger reduction in fracture energy release. Also, as in the case of elastic mismatch, the relative thickness sensitivity under peel load is much higher than that under shear.

From the perspective of debonding resistance, one would thus prefer to have a bond line that has a stiffness close to that of the adjoining concrete and a thin epoxy bond line when a considerably strong elastic mismatch is present, so as to minimize fracture energy release. On the other hand, for a given set of constituent materials, one would however prefer to have a thicker epoxy bond and a thinner FRP laminate so that the debonding driving force is minimized. The results of this parametric study indicate that the design
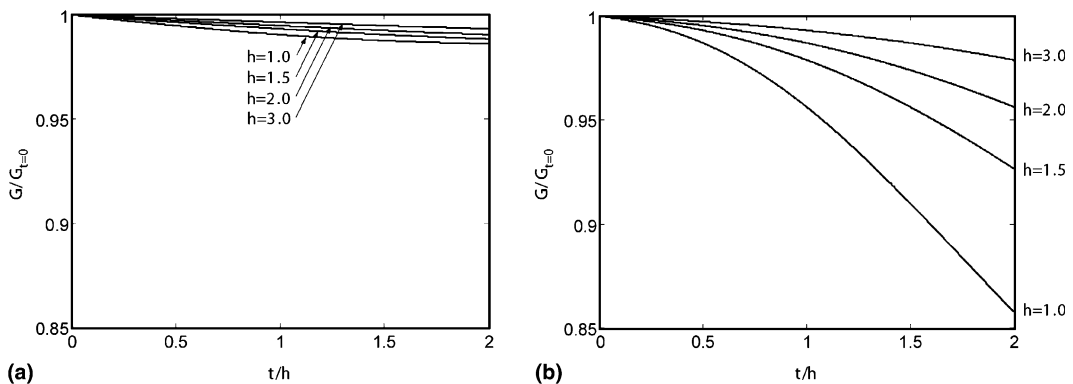

Fig. 8. Effect of epoxy thickness on (a) shear G and (b) peel G.

of a FRP retrofitted system against debonding is a complex problem that will require parametric optimization.

7. Correlation of derived G and mixed-mode stress intensities

As mentioned earlier, the derived fracture models describe only the total interface fracture energy without explicit consideration of the mixed-mode stress-intensities at the crack tip, which could be very useful in interpreting the debonding locus of the retrofitted system [1,21]. Although possible, derivation of explicit expressions of the mode-mix quantification of the tri-layer problem will however require very involved elasticity analyses that include solving integral equations of the crack problem even for the bi-layer case [20]. Yet, considerations of such mode-mix behavior (i.e. determination of the opening and shearing mode stress intensities) can instead be performed numerically by means of the practical yet robust M-integral technique developed by Matos et al. [27] that makes use of the finite element (F.E.) fracture analysis method. This method involves first computing the J-integral using the virtual crack extension method, followed by numerical adjustments of the displacement fields for respectively the opening mode and the shearing mode. This adjustment is needed due to the fact that when evaluating the path integrals for the interface fracture problem involving adjoining materials, the displacements solution in one material does not satisfy the governing equations in the other, and so the symmetric and anti-symmetric parts are invalid displacements in both materials. As a result of the numerical procedure, stress intensities K_I^* (open mode) and K_{II}^* (shear mode) can be correctly obtained. The quantities are related to the derived G as follows:

$$G = \frac{K_I^{*2} + K_{II}^{*2}}{E^* \cosh^2(\pi \varepsilon)} \tag{28}$$

where

$$\frac{1}{E^*} = \frac{1}{2}\left(\frac{1}{\overline{E}_{\text{upper}}} + \frac{1}{\overline{E}_{\text{lower}}}\right) \tag{28a}$$

$$\varepsilon = \frac{1}{2\pi} \ln\left(\frac{1 - \beta_{\text{Dundurs}}}{1 + \beta_{\text{Dundurs}}}\right) \tag{28b}$$

As verification of the derived G model, the values of K_I^* and K_{II}^* are computed and the G is numerically back calculated and compared with the value obtained from the derived G model. Verification is performed on Case 2 peel and shear fracture models respectively using common material and geometric data of a typical retrofitted joint. The values are summarized in Table 6. For the derived G model, bond width B is set at 25 mm. For both models, bond length is set at 150 mm, and N_x and N_y are, respectively, 20 kN and 70 N.

The finite element fracture model consists of eight-node isoparametric plain strain elements throughout. In the crack tip region, mid-side nodes are moved to the quarter-point positions to force $1/\sqrt{r}$ singularity for the herein linear elastic consideration. A total of eight rings of 256 elements form the crack tip region, which had an overall size of 0.8 mm × 0.8 mm. The G values are evaluated only from the outer four rings, as it is a known property that near-tip computed G values are not as accurate ([27]) due to the inherent nature

Table 6
Model parameters

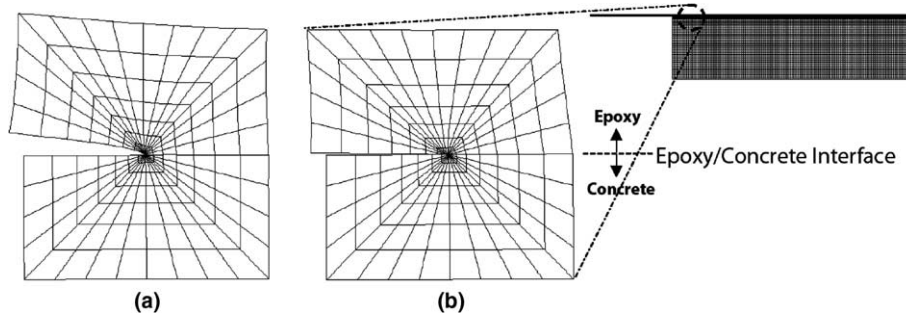|	Elastic modulus (GPa)	Poisson's ratio	Thickness (mm)
FRP	148.0	0.27	1.28
Epoxy	1.5	0.35	1.00
Concrete	21.8	0.19	37.50

Fig. 9. Deformed meshes of the crack tip region under (a) peel and (b) shear.

Table 7
Derived G vs. numerical G values

	G_{peel} (kJ/m^2)	G_{shear} (kJ/m^2)
Derived G model	0.4401	1.5561
	0.4400	1.5584
F.E. G computation	($K_I^* = 35.58$ MPa$\sqrt{mm}$	($K_I^* = 23.99$ MPa$\sqrt{mm}$
	$K_{II}^* = -13.56$ MPa$\sqrt{mm}$)	$K_{II}^* = -67.52$ MPa$\sqrt{mm}$)

of the mathematical formulation. Fig. 9 shows the deformed meshes of the crack tip region for each respective loading case.

Table 7 provides a summary of the values obtained from Eqs. (25) and (23), respectively, for the peel and shear case and from the finite element computation.

Excellent agreement on the G values for both cases has been achieved. Note also from the values of K_I^* and K_{II}^* as well as the deformed meshes in Fig. 9 that the mode mix behavior is substantial for both cases, although the models are loaded, respectively, under an apparent peel and shear configuration.

Also, it can be stated that, in view of the robustness of the derived G models, the developed methodology can be used as an effective and convenient means in conjunction with other analytical tools such as the crack kinking criterion [18] in further studying the debonding phenomenon in FRP retrofitted layered material system.

8. Conclusion

Debonding in FRP plated concrete structures is a complex phenomenon that may involve failure propagation within the concrete substrate, inside the adhesive, in the form of FRP delamination, FRP/epoxy interface separation, and epoxy/concrete interface separation, totaling five distinct debonding modes. These different failure modes are partly attributed to the fact that the adhesive bond line thickness is relatively large such that quantification of the problem requires a tri-layer interface fracture treatment that can account for the material and geometric information of all three constituent material layers in the FRP bonded concrete system.

Motivated by this rationale, this paper develops a tri-layer fracture energy release rate model to accurately and precisely quantify the debonding problem. Using the linear elastic assumption, energy arguments, and the classical beam theory, the total interface fracture energy release rate, G, is rigorously derived by evaluating the difference in strain energy far behind and far ahead of the crack tip. The full

set of tri-layer *G* solutions for five idealized plain-strain debonding cases, which correspond to the five debonding modes is presented. These newly derived models contain fairly general boundary conditions, making them applicable to many different physical interface fracture models that may be used to quantify debonding in FRP retrofitted concrete.

In particular, the derived models are specialized to describe peel and single lap shear debonding fracture that is commonly encountered in the retrofitted material systems. The specialized fracture models can be used to compute the interface fracture toughness of the fracture samples loaded under peel and shear configurations using critical loads determined from fracture tests as inputs. Also, since the material and geometric parameters are explicitly expressed in the *G* models, extensive parametric studies can be performed for design purposes through parametric optimization. The accuracy of the model is validated by comparing the values of *G* computed from the two specialized models with those obtained numerically from a finite element fracture analysis. Excellent agreements are obtained. The robustness of the derived *G* model makes it an effective and convenient means in investigating the debonding phenomenon in FRP retrofitted layered material system.

Acknowledgements

Appendix A

h = Layer 1 thickness, t = Layer 2 thickness, H = Layer 3 thickness

$$\Sigma_{mn} = \frac{\overline{E}_m}{\overline{E}_n} \quad \text{where } m, n = 1, 2, 3$$

$$\eta = \frac{h}{H}, \quad \gamma = \frac{t}{H}, \quad \xi = \frac{1}{\eta}, \quad \xi_i = \frac{H_i}{h} \quad \text{where} \quad i = 1, 2, 3$$

$$\alpha = \frac{\Sigma_{23}\gamma(2+\gamma)+1}{2\eta(1+\Sigma_{23}\gamma)}$$

$$\alpha_3 = \frac{(\eta\xi_3)^2 + \Sigma_{23}\gamma(2\eta\xi_3+\gamma) + \Sigma_{13}\eta(2\eta\xi_3+2\gamma+\eta)}{2\eta(\eta\xi_3+\Sigma_{23}\gamma+\Sigma_{13}\eta)}$$

$$\delta = \frac{\Sigma_{12}+2\Sigma_{12}\frac{\gamma}{\eta}+\left(\frac{\gamma}{\eta}\right)^2}{2\left(\Sigma_{12}+\frac{\gamma}{\eta}\right)}$$

$$\Delta = \frac{1+\Sigma_{23}\gamma(2+\gamma)+\Sigma_{13}\eta(2+2\gamma+\eta)}{2\eta(1+\Sigma_{23}\gamma+\Sigma_{13}\eta)}$$

$$\Delta_2 = \frac{\Sigma_{12}\left(1 + 2\frac{\gamma}{\eta} - 2\xi_2\right) + \left(\frac{\gamma}{\eta} - \xi_2\right)^2}{2\left(\Sigma_{12} + \frac{\gamma}{\eta} - \xi_2\right)}$$

$$\Delta_3 = \frac{1 + \Sigma_{23}\gamma(2 + \gamma) + \Sigma_{13}\eta\xi_1(2 + 2\gamma + \eta\xi_1)}{2\eta(1 + \Sigma_{23}\gamma + \Sigma_{13}\eta\xi_1)}$$

$$\Delta_{33} = \frac{1 + \Sigma_{23}\xi_2\eta(2 + \xi_2\eta)}{2\eta(1 + \Sigma_{23}\xi_2\eta)}$$

References

[1] Au C. Moisture degradation in FRP bonded concrete systems: an interface fracture approach. Sc.D. Thesis, Massachusetts Institute of Technology, Cambridge, MA; 2004.
[2] Bizindavyi L, Neale KW. Transfer lengths and bond strengths for composites bonded to concrete. J Compos Construc 1999;3(4):153–60.
[3] Büyüköztürk O. Fracture mechanics parameters influencing the mechanical properties of concrete composites. In: Sih George C, editor. Advanced technology for design and fabrication of composite materials and structures. Kluwer Academic Publishers; 1995. p. 319–31.
[4] Büyüköztürk O, Hearing B. Failure behavior of precracked concrete beams retrofitted with FRP. J Compos Construc 1998;2(3):138–44.
[5] Büyüköztürk O, Lee KM. Assessment of interfacial fracture toughness in concrete composites. J Cement Concr Compos 1993;15:143–51.
[6] Büyüköztürk O, Gunes O, Karaca E. Progress review on understanding debonding problems in reinforced concrete and steel members strengthened using FRP composites. J Construc Building Mater 2004;18:9–19.
[7] Chajes MJ, Finch WW, Januszka TF, Thomson TA. Bond and force transfer of composite material plates bonded to concrete. ACI Struct J 1996;93(2):208–17.
[8] Chajes MJ, Thomson Jr TA, Farschman CA. Durability of concrete beams externally reinforced with composite fabrics. Construc Building Mater 1995;9(3):141–8.
[9] Chen JF, Teng JG. Anchorage strength models for FRP and steel plates bonded to concrete. J Struct Engrg 2001;127(7):784–91.
[10] Dundurs J. Edge-bonded dissimilar orthogonal elastic wedges. J Appl Mech 1969;36:650–2.
[11] Gao B, Kim JK, Leung CKY. Effect of rubber modifier on interlaminar fracture toughness of CFRP-concrete interface. Compos Sci Technol 2003;63:883–92.
[12] Garden HN, Hollaway LC. An experimental study of the failure modes of reinforced concrete beams strengthened with prestressed carbon composite plates. Composites Part B 1998;29(4):411–24.
[13] Garden HN, Hollaway LC. An experimental study of the influence of plate end anchorage of carbon fiber composite plates used to strengthen reinforced concrete beams. Compos Struct 1998;42(2):175–88.
[14] Gdoutos EE, Pilakoutas K, Rodopoulos CA, editors. Failure analysis of industrial composite materials. McGraw-Hill; 2000.
[15] Grace NF. Concrete repair with CFRP. Concrete International 2004(May):45–52.
[16] Gunes O. A fracture based approach to understanding debonding in FRP bonded structural members, Ph.D. Thesis, Massachusetts Institute of Technology, Cambridge, MA; 2004.
[17] Hassanen MAH, Raoof M. Design against premature peeling failure of RC beams with externally bonded steel or FRP plates. Mag Concr Res 2001;53(4):251–62.
[18] He MY, Hutchinson JW. Kinking of crack out of an interface. J Appl Mech 1989;56:270–8.
[19] Hutchinson JW. Mechanics of thin films and multilayers. Lecture notes: solid mechanics. Technical University of Denmark; 1996.
[20] Hutchinson JW, Suo Z. Mixed mode cracking in layered materials. Adv Appl Mech 1992;29:63–191.
[21] Infrastructure Science and Technology (IST) Group. Failure behavior of FRP bonded concrete affected by interface fracture. IST Group website, <http://web.mit.edu/istgroup> 2004.
[22] Karbhari VM, Zhao L. Issues related to composite plating and environmental exposure effects on composite—concrete interface in external strengthening. Compos Struc 1998;40(3–4):293–304.
[23] Karbhari VM, Engineer M, Eckel II DA. On the durability of composite rehabilitation schemes for concrete: use of a peel test. J Mater Sci 1997;32(1):147–56.

[24] Khalifa A, Nanni A. Improving shear capacity of existing RC T-section beams using CFRP composites. Cement Concr Compos 2000;22:165–74.

[25] Khalifa A, Gold WJ, Nanni A, Aziz AMI. Contribution of externally bonded FRP to shear capacity of RC flexural members. J Compos Construc 1998;2(4):195–202.

[26] Kimpara I, Kageyama K, Suzuki T, Osawa I, Yamaguchi K. Characterization of debonding energy release rate of FRP sheets bonded on mortar and concrete. Adv Compos Mater 1999;8(2):177–87.

[27] Matos PPL, McMeeking RM, Charalambides PG, Drory MD. A method for calculating stress intensities in bimaterial fracture. Int J Frac 1989;40:235–54.

[28] Meier U. Carbon fiber reinforced polymers, modern materials in bridge engineering. Struc Engrg Int 1992;2(1):7–12.

[29] Mukhopadhyaya P, Swamy RN, Lynsdale CJ. Influence of aggressive exposure conditions on the behavior of adhesive bonded concrete—GFRP joints. Construc Building Mater 1998;12:427–46.

[30] Nakaba K, Kanakubo T, Furuta T, Yoshizawa H. Bond behavior between FRP laminates and concrete. ACI Struc J 2001;98(3):359–67.

[31] Neubauer U, Rostasy FS. Design aspects of concrete structures strengthened with externally bonded FRP-plates. In: Proceedings of the seventh international conference on structural faults and repair, vol. 2, Edinburgh, UK; 1997. p. 109–18.

[32] Sharif A, Al-Sulaimani GJ, Basunbul IA, Baluch MH, Ghaleb BN. Strengthening of initially loaded reinforced concrete beams using FRP plates. ACI Struct J 1994;91(2):160–8.

[33] Smith ST, Teng JG. Interfacial stresses in plated beams. Engrg Struct 2001;23(7):857–71.

[34] Taljsten B. Strengthening of beams by plate bonding. J Mater Civil Engrg 1997;9(4):206–11.

[35] Toutanji HA, Gomez W. Durability characteristics of concrete beams externally bonded with FRP composite sheets. Cement Concr Compos 1997;19:351–8.

[36] Triantafillou TC, Plevris N. Strengthening of RC beams with epoxy-bonded fibre-composite materials. Mater Struct 1992;25:201–11.

[37] Wu Z, Yuan H, Niu H. Stress transfer and fracture propagation in different kinds of adhesive joints. J Engrg Mech 2002;128(5):562–73.